Supplementary Information:

Assessing the Potential of Non-pyrophoric $Zn(DMP)_2$ for the Fast Deposition of ZnO Functional Coatings by Spatial Atomic Layer Deposition

L. Johnston [a], J. Obenlüneschloß [b], M.F. Khan Niazi [a], M. Weber [a], C. Lausecker [a], C. Velasquez Sanchez [a], L. Rapenne [a], H. Roussel [a], D. Bellet [a], A. Devi [b,c], D. Muñoz-Rojas [a,*].

[a]*Univ. Grenoble Alpes, Grenoble INP, CNRS, LMGP - Grenoble (France)*

[b]*Ruhr Univ. Bochum, Inorganic Materials Chemistry, 44801 - Bochum (Germany)*

[3]*Leibniz Institute for Solid State and Materials Research, 01069, Dresden - (Germany)*

*Corresponding author. Email: david.munoz-rojas@grenoble-inp.fr

Table of Contents

Process parameters

Two processes have been probed and are hereafter named as follows. The “low saturation” process at T_B = 60 °C was tested initially and was later improved upon using the “high saturation” process, which features a higher bubbler temperature of T_B = 90 °C, a stronger nitrogen gas barrier and bubbling flow in the $Zn(DMP)_2$ bubbler, while also being performed at higher substrate speeds, in order to maximize deposition throughput. Though most of the described parameters are optimized to produce more saturated ALD monolayers and thus more conformal films, parameters such as the nitrogen gas barrier flow were optimized to minimize precursor mixing in the gas phase producing uncontrolled CVD deposition.

SALD Process	N_2 carrier gas flow rates (SCCM)					Other parameters	
	$Zn(DMP)_2$ (2 regions)		H_2O (3 regions)		N_2 (6 regions)		
	Bubbler ($Q_{B,M}$)	Dilution ($Q_{D,M}$)	Bubbler ($Q_{B,O}$)	Dilution ($Q_{D,O}$)	Direct (Q_N)	Substrate speed (v_S)	Bubbler T (T_B)
Low saturation	50	250	150	300	900	3.1 cm/s	**60 °C**
High saturation	100	200	150	300	2000	4.0 cm/s	**90 °C**

Table S1: Parameters for the study of $Zn(DMP)_2/H_2O$ SALD. Two processes are explored: the low saturation process wherein the bubbler is heated to 60 °C; while the high saturation process used a temperature of 90 °C instead, significantly increasing the $Zn(DMP)_2$ evaporation rate and thus the $Zn(DMP)_2$ partial pressure in the metal precursor region of the SALD.

Samples produced through the high saturation process were characterized in the case of the GPC and growth rates versus temperature (where the thickness was measured ex-situ using ellipsometry), in the XRR-derived density measurements, and the GI-XRD studies, while the low saturation process was used to produce the XPS-studied sample, to provide the LCA data, and to coat the AgNW networks. Both processes yielded similar densities using XRR in the vicinity of 140 °C as shown in Figure 7 and similar crystallinity overall as per Figure 8, and the high saturation process was found to yield similar films from 140 to 180 °C by these same standards.

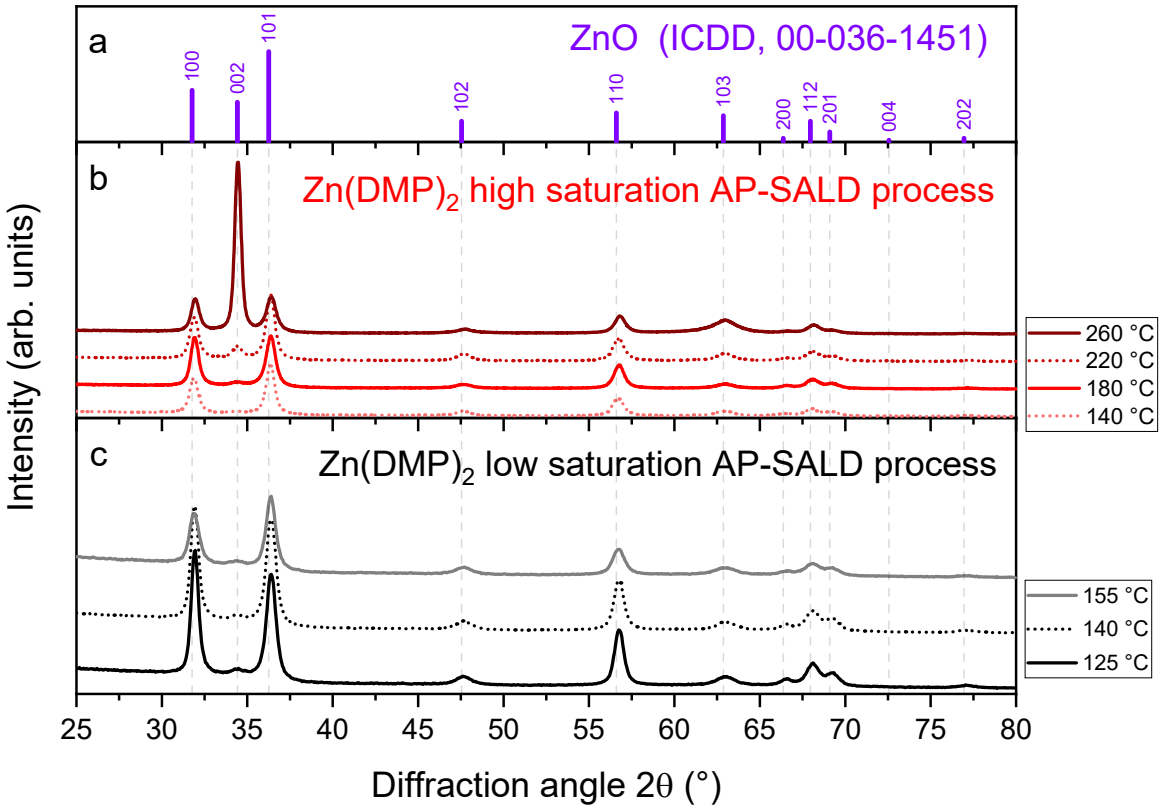

Figure S1: GI-XRD patterns of ZnO thin films deposited at various temperatures using the AP-SALD processes described previously compared with the theoretical powder diffraction pattern for ZnO in the wurtzite structure as per the ICDD database (a). The high saturation (b) and low saturation (c) AP-SALD processes show mainly a-axis growth for all temperatures except 260 °C where c-axis growth was achieved. SEM surface morphologies are displayed for the high saturation process at 260 °C (d) and 180 °C (e), and also for the "low saturation" process at 140 °C (f). All samples investigated via SEM had thicknesses between 65 and 95 nm approximately.

The naming of these processes as high and low saturation stemmed from the observed GPC vs. deposition temperature curves observed. Assuming the H_2O pulse saturated the surface during each ALD cycle, the discrepancy visible between the two open-air SALD processes in the intermediate GPC values shows that in one process the $Zn(DMP)_2$ ALD half-cycle reached a lower saturation (which we may define as the surface coverage attained during the elapsed time of the precursor pulse) than the other (justifying the "high/low saturation" denomination) likely because of the smaller partial pressure of precursor in the gas reaching the surface. Though the low saturation process yielded a highly controlled thickness at a lower bubbler temperature in the case of thin films, this process may produce non-conformal coatings in the case of high aspect ratio substrates as in such cases, the precursor will fail to reach deeper regions of the substrate as easily as the topmost regions. Meanwhile the high saturation process reached GPC values similar to the literature found on other instances of $Zn(DMP)_2$ ALD at 140 °C which indicates it could still reach a similar ALD saturation than other techniques.[1]

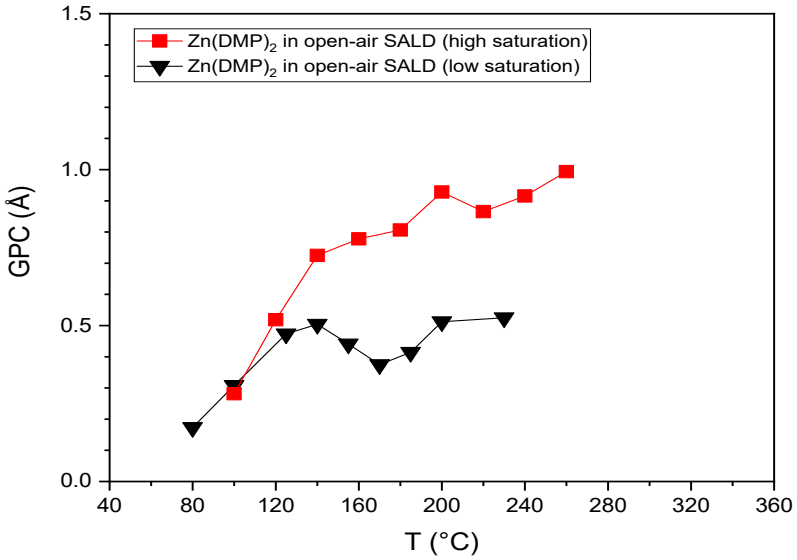

Figure S2: GPC vs. deposition temperature for both open-air SALD processes tested using $Zn(DMP)_2$

Growth rate methodology

Since the size of the sample will obviously affect the duration of the deposition, the method used to convert a GPC (Å per cycle) value into a growth rate (Å per minute) must be clearly established. This is the case both in conventional ALD (duration of precursor pulse necessary to saturate the deposition surface) as well as SALD (where the fixed speed implying an inverse relation between sample length and SALD cycle duration).

As such, in SALD, two critical values govern the efficiency and speed of the process: the sweeping speed of the sample relative to the SALD head (v_S); and the spatial period of one ALD cycle along the SALD head (Λ). This latter parameter can correspond to the distance between two same precursor lines. The simplest law emanating from these two values is to consider an SALD head performing a single ALD cycle along an infinitely long sample. In this scenario, a single thickness equal to the GPC is coated each time a distance Λ is travelled by the head at a speed v_S. Giving us the idealised law for the growth rate (GR) as

Equation S1

$$GR = GPC \cdot \frac{v_S}{\Lambda}$$

which is exact for circular SALD systems where the substrate is rotated to sequentially expose the surface to different gas regions, but functions instead as a maximal growth rate for linear SALD. This is due to the fact that at the edge of the deposited region, as the SALD head begins to retrograde in its oscillation, a partial deposition occurs as a consequence of incomplete SALD passes. As such, though the central region will observe the passing of 4 metal precursor exposures during on SALD head oscillation (in our setup, the head has 2 such lines and passes twice to produce one oscillation), the outermost region will only see a single such exposure during an entire oscillation.

This leads to an excess trivial region to account for when considering the distance that the head must travel to uniformly coat a sample of interest with length d. Coating this distance with the previously fixed speed while accounting for the extra trivial region can be shown to result in the following law (for a palindromic head with n metal precursor lines and $n+1$ oxygen precursor lines).

Equation S2

$$GR = n \cdot GPC \cdot \frac{v_S}{(2n-1)\Lambda + d}$$

Notably, these laws only take into account one of the substrate dimensions, which is expected as the only limiting factors in the other direction are the width of the SALD head and the evaporation rate of the precursor (which may need to be increased to provide the same vapor pressure to a larger region). In all instances, equation S1 is used to provide a maximal value and to allow easier comparison between SALD processes. In our setup, we used a speed v_S = 40 mm/s with an SALD head such that Λ = 10.5 mm to produce a GPC of 0.7 Å, giving us a maximal growth rate of 184 Å/min.

XRR density methodology

ZnO density is determined from the critical angle θ_c, which is directly related to the electron density ρ_e in the material (which is assumed to be homogeneous) as follows.

Equation S3

$$\rho_e = \frac{\pi\theta_c^2}{\lambda^2 r_e}$$

With θ_c given in radians, λ the X-ray wavelength which was 1.54 Å in our experiments, and the classical electron radius $r_e = 2.82 \cdot 10^{-15}$ m.[2] This electron density can in turn be used to express the ZnO mass density ρ_{ZnO} by a factor as

Equation S4

$$\rho_{ZnO} = \frac{M_{ZnO}}{N_A Z_{ZnO}} \rho_e$$

Where the molar mass of ZnO M_{ZnO} is 81.4 g/mol, N_A is Avogadro's constant, and Z_{ZnO} is the number of moles of electrons per mole of ZnO, or the sum of atomic numbers in ZnO, *i.e*. 38.

To define the critical angle θ_c, the XRR curves are normalised by a reference intensity I_0 corresponding to the intensity plateau in the total reflection region below the critical angle, and the plateau length depends on the physical length of the substrate along the direction of the X-ray beam. Our critical angle can be considered the angle at which the normalized intensity drops to $\frac{I_0}{2}$ after the total reflection plateau.

The error bars for the estimated densities are obtained graphically by considering that the "real" transition point is necessarily within $\frac{I_0}{2}$ ± 0.1 (as displayed in the figure inset). This leads to an error that depends on the steepness of the intensity slope at the $I = \frac{I_0}{2}$ transition point, which was sufficiently steep in all cases to reduce the error to at most ± 0.10 g/cm³, except for the sample deposited at 155 °C with the "low saturation" process, whose intensity slope at the critical angle was weaker resulting in an error around ± 0.16 g/cm³.

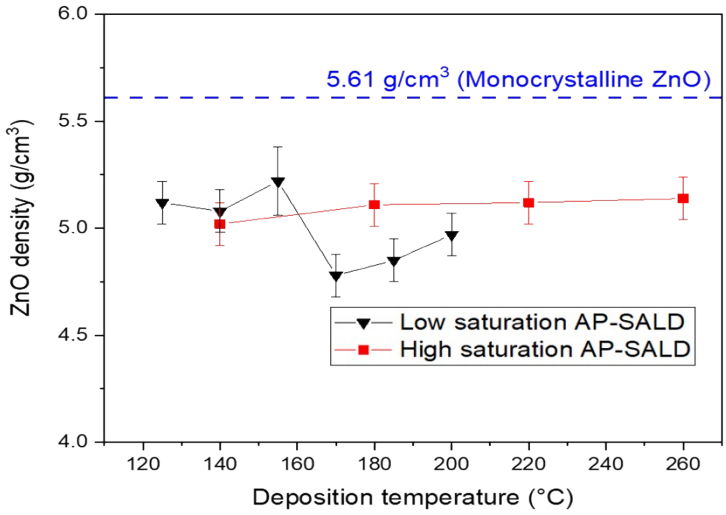

Figure S3: XRR-derived density of ZnO thin-films as a function of deposition temperature and deposition process used.

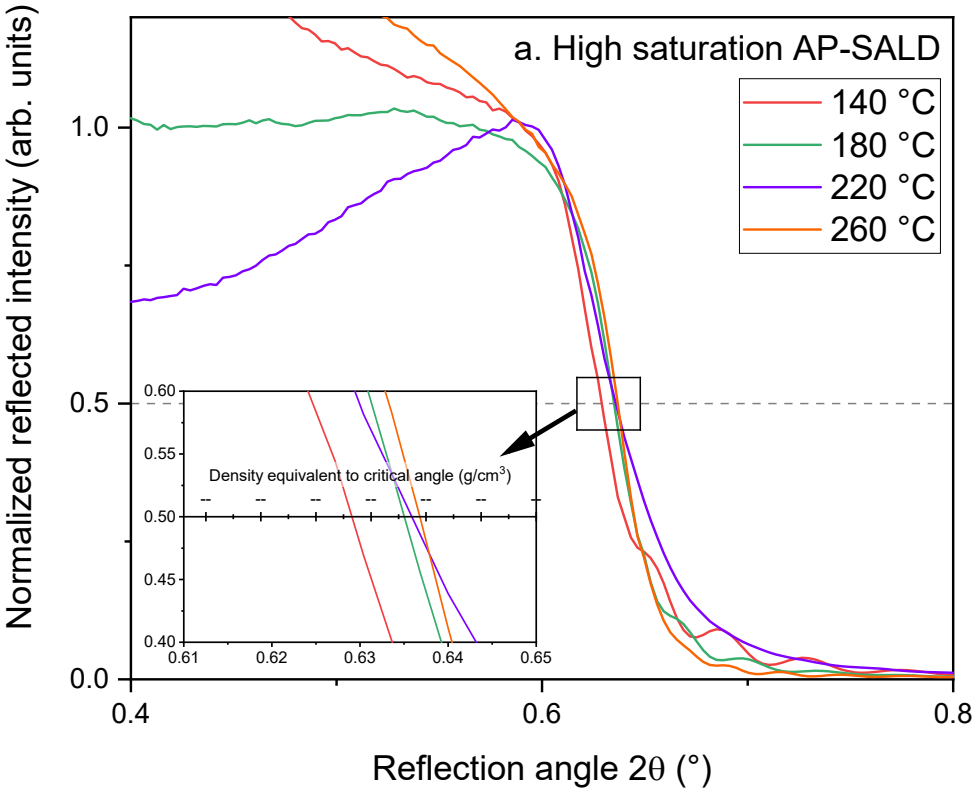

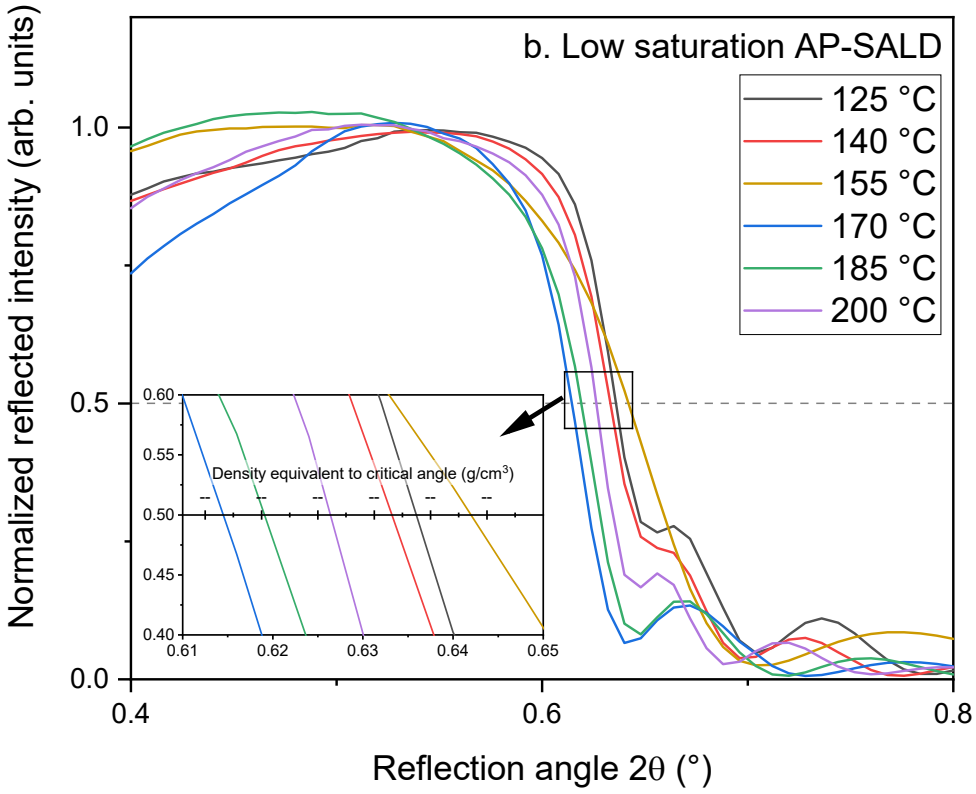

Figure S4: XRR curves around critical angle for "low saturation" (a) process and "high saturation" process (b).

Saturation study vs. substrate speed

The ALD saturation as a function of time, which we may define as the extent to which total surface coverage is achieved during each ALD cycle for the relevant precursor(s), typically follows a bounded exponential law in the case of monolayers as per

Equation S5

$$GPC = Ae^{-t/B}$$

with *A* the growth per cycle (GPC) at saturation and *B* a coefficient corresponding to the precursor characteristic adsorption time, while *t* is the precursor/surface exposure time (or the precursor pulse time). By definition, the limit of the GPC as *t* goes to infinity tends towards *A*. Since in SALD we may not individually vary one of the pulse times while keeping the co-reactant pulse time constant as in conventional ALD, we prefer to consider overall cycle time. Functioning under the hypothesis that the water pulse always saturates the surface with hydroxyl surface species faster than the $Zn(DMP)_2$ pulse saturates it in adsorbed Zn precursor, we may expect the evolution of the GPC to only reflect a change in the achieved surface coverage during the Zn precursor pulse, allowing us to model this trend with equation S5.

Due to the narrow range of speeds that could be tested with the SALD setup used in this study, the data was highly variable and thus fitting an exponential law required a wide confidence interval. This resulted in the graph below for different temperatures in the high saturation AP-SALD process.

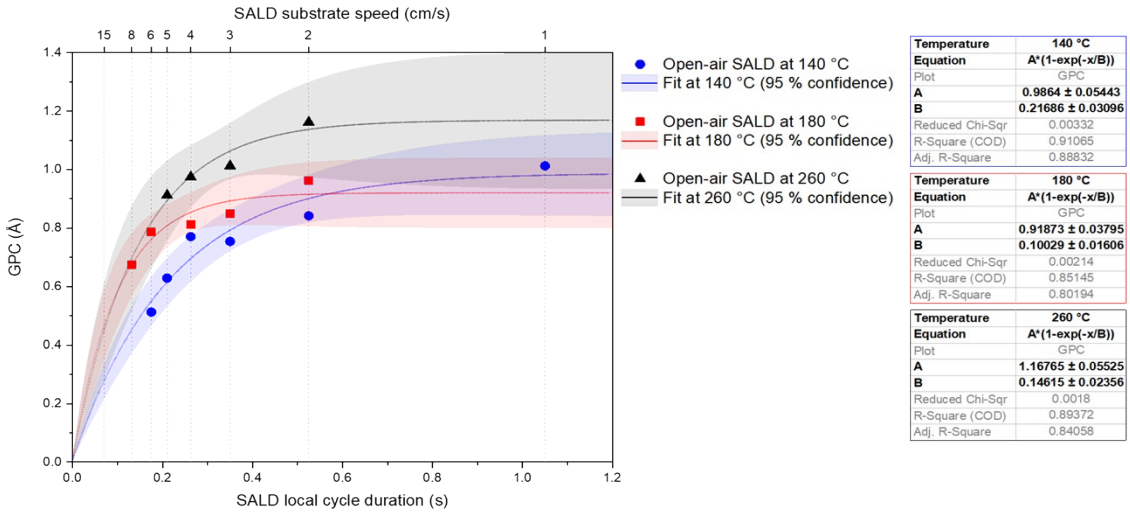

Temperature	140 °C
Equation	A*(1-exp(-x/B))
Plot	GPC
A	0.9864 ± 0.05443
B	0.21686 ± 0.03096
Reduced Chi-Sqr	0.00332
R-Square (COD)	0.91065
Adj. R-Square	0.88832

Temperature	180 °C
Equation	A*(1-exp(-x/B))
Plot	GPC
A	0.91873 ± 0.03795
B	0.10029 ± 0.01606
Reduced Chi-Sqr	0.00214
R-Square (COD)	0.85145
Adj. R-Square	0.80194

Temperature	260 °C
Equation	A*(1-exp(-x/B))
Plot	GPC
A	1.16765 ± 0.05525
B	0.14615 ± 0.02356
Reduced Chi-Sqr	0.0018
R-Square (COD)	0.89372
Adj. R-Square	0.84058

Figure S5: Growth per cycle (GPC) for differing precursor exposure times in the high saturation AP-SALD process for several substrate temperatures. Langmuir isotherms are used to approximately fit expected saturated GPC.

The data fitting shows that the deposition at 180 °C saturated much faster than at 140 °C, hinting towards a mostly chemisorption-based adsorption process for $Zn(DMP)_2$ around these temperatures. This is because higher temperatures tend to increase the chemisorption probability, whereas with physisorption processes, higher temperatures tend to increase desorption probability due to the higher thermal (and thus kinetic) energy of the physiosorbed species.[3] Since physisorption processes do not yield self-limited monolayer-type growth, they are generally not accepted as ALD processes. As such, the increase of adsorption rate with temperature hints at an ALD window between 140 °C and 180 °C at least, and equation S5 can be used to estimate the saturated GPC. This places our experiments at 180 °C roughly around 87% surface saturation when using a substrate speed of 4 cm/s, which may be insufficient for certain high aspect ratio substrates but should still result in sufficient conformality, homogeneity, and thickness control in the vast majority of applications, while maintaining high growth rates.

These results are consistent with the results from Stefanovic *et al*. in similar experiments with $Zn(DMP)_2$, though Mai *et al*. suggested the decomposition of $Zn(DMP)_2$ could produce spurious CVD deposition using oxygen plasma-enhanced ALD above 180 °C,[4] which may also be present here in lesser amounts due to the lower saturation standard.

Film homogeneity by SEM for 180 at 260 °C

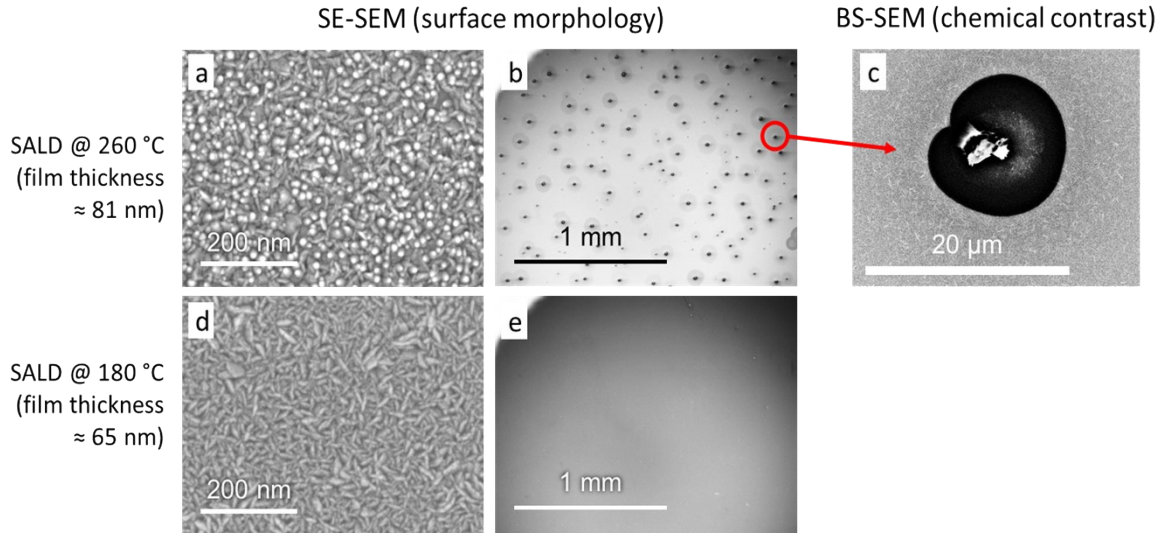

Figure S6: Surface morphology (Secondary electrons SEM) at nanoscale (a, d) and at macroscopic scale (b, e) of films deposited at 260 °C (a, b) and 180 °C (d, e) using "high saturation" process. The microscopic particle defects obtained at 260 °C were further studied using back-scattered electrons (c).

In plasma-enhanced ALD experiments from Mai *et al.*, a precursor decomposition phenomenon was attributed to a steep GPC rise above 180 °C. Considering this as a possibility in our depositions at these temperatures, we studied the surface morphology for a pair of temperatures below and above this postulated decomposition point. Though no steep rise could be observed in our AP-SALD experiments, possibly due to the shorter precursor pulse times in AP-SALD, the presence of microparticles roughly 10—20 µm in size could still be noticed in the samples deposited at 260 °C. These particles were also studied with back-scattered SEM, for which the particles yielded less signal, indicating a region of matter composed of nuclei with lower atomic numbers Z. Considering the organometallic nature of the precursor used, we may assume these microparticles are mostly composed of aggregated precursor fragments after thermal decomposition.

XPS additional data and fitting

Table S2: Quantification of XPS of sample at 150 °C

Atom (Orbital)	Zn ($2p_{3/2}$)	O (1s)		C (1s)	
Atom chemical environment	**Zn in ZnO lattice**	**Other O species (OH, O^-)**	**O^{2-} in ZnO lattice**	**C=O**	**C-C, C-H**
Peak BE (eV)	1021.69	532.07	530.53	289.92	285.45

FWHM (eV)	1.52	1.56	1.26	2.37	2.08
Area (CPS · eV)	$9.44 \cdot 10^5$	$4.01 \cdot 10^4$	$1.49 \cdot 10^5$	$1.32 \cdot 10^3$	$1.95 \cdot 10^3$
Atomic %	**42.26**	**11.78**	**43.63**	**0.94**	**1.39**

Details on the performed LCA analysis

Life Cycle Assessment (LCA) is a comprehensive analysis methodology that assesses the associated environmental impact of a product/production system from its creation to its disposal, considering all upstream and downstream processes involved. LCA follows a standardized procedure in accordance with the ISO Standard (ISO 14044:2006), which includes 4 major steps: goal and scope definition, inventory analysis, impact assessment and interpretation.[5]

The LCA performed followed the same procedure as the ones we performed in previous work.[6] The functional unit chosen for this study is the "deposition of a 20 nm film from a Zn precursor and water on an 80 cm^2 substrate surface". The area of 80 cm^2 corresponds to a typical 4-inch wafer. This functional unit was selected to allow for a direct comparison of the SALD process studied with research previously published on ALD. The LCA study follows the Type B systems approach as established by Bauer C. *et al*.,[7] which is used to compare two different manufacturing alternatives performing the same function.

The system boundaries for this study are defined as cradle-to-gate, including life cycle phases from raw material extraction to the point of leaving the factory gate. To produce a ZnO film via SALD, multiple inputs are required, including specialized equipment, specific precursor gases, and energy (electricity). The SALD reactor considered is based on a close proximity approach and is the one used in our laboratory. The schematic below depicts the design of the reactor considered.

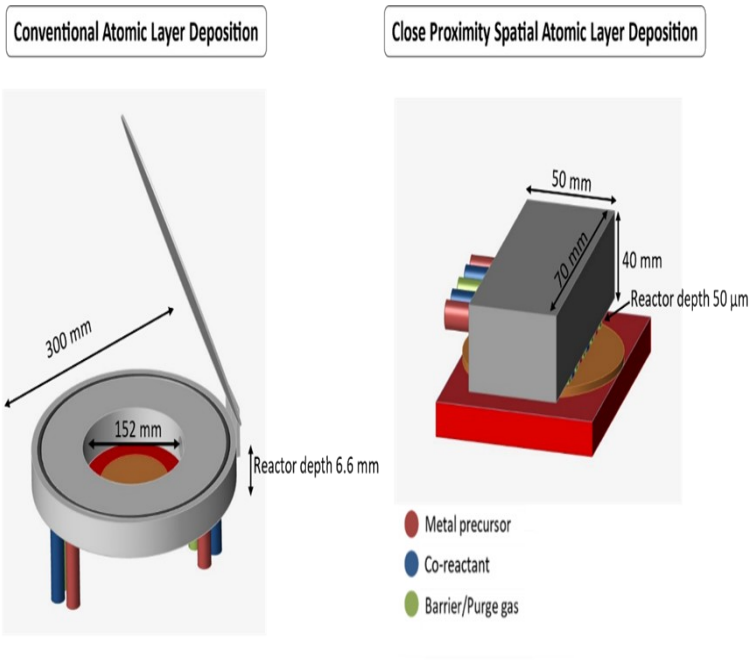

Figure S7: Schematic representation of the SALD reactor considered for this LCA study.

The inventory of SALD equipment was established through the measurement or estimation of the materials needed for constructing the equipment utilized in our laboratory. In comparison to ALD, SALD equipment comprises more components in the high wear segment due to the manifold head's shorter lifespan, which is prone to clogging or blocking after a certain number of depositions. Detailed information about the SALD equipment inventory has been previously documented in published works. [6]

Utilizing the open-source software OpenLCA, we documented all material and energy inputs pertinent to the involved processes. In this study, the Ecoinvent 3.8 database supplied machine and energy Life Cycle Inventory (LCI) data. However, the availability of datasets on metal-organic precursors like $Zn(DMP)_2$ is limited within LCI databases. Consequently, we opted to "synthesize" these precursors using their base chemicals and reactions present in the Ecoinvent 3.8 database. This approach emphasizes environmental impacts, which might be overlooked if a chemically similar substance already present in the database is substituted. For this evaluation, the chosen energy provider was RER (Europe in Ecoinvent), providing an overview of the deposition process in Europe. The tables below provide a comprehensive breakdown of the inputs considered for the LCA of SALD processes and the synthesis of DEZ and $Zn(DMP)_2$.

Inputs/Outputs: SALD of zinc Film (Zn(DMP)2) PP France - FR

Inputs

Flow	Category	Amount	Unit		Provider
BDMPZ, Zn(DMP)2 (...	SALD/chemicals	1.81000E-5	kg		BDMPZ, Zn(DMP)2
electricity, low voltage	351:Electric power gen...	1.08600	MJ		market for electricity, low voltage | electricity, low voltage | Cutoff, S - FR
nitrogen, liquid	201:Manufacture of b...	0.03900	kg		market for nitrogen, liquid | nitrogen, liquid | Cutoff, S - RER
SALD Machine	SALD/Machines	0.00010	Item(s)		SALD Machine - FR
SALD machine parts ...	SALD/Machines	1.00000E-5	Item(s)		SALD Machine parts (low wear) - FR
water, deionised	360:Water collection, t...	4.36000E-5	kg		market for water, deionised | water, deionised | Cutoff, S - Europe without Switzerland

Figure S8: LCA detail: SALD process with $Zn(DMP)_2$ and water

Inputs/Outputs: SALD of zinc Film PP - FR

Inputs

Flow	Category	Amount	Unit	C...	Provider
Diethyl Zinc	SALD/chemicals	1.06000E-5	kg		Diethyl Zinc
electricity, low voltage	351:Electric power gen...	0.92500	MJ		market group for electricity, low voltage | electricity, low voltage | Cutoff, S - RER
nitrogen, liquid	201:Manufacture of b...	0.00777	kg		market for nitrogen, liquid | nitrogen, liquid | Cutoff, S - RER
SALD Machine	SALD/Machines	0.00010	Item(s)		SALD Machine - FR
SALD machine parts ...	SALD/Machines	1.00000E-5	Item(s)		SALD Machine parts (low wear) - FR
water, deionised	360:Water collection, t...	8.20000E-6	kg		market for water, deionised | water, deionised | Cutoff, S - Europe without Switzerland

Figure S9: LCA detail: SALD process with DEZ and water

Inputs/Outputs: BDMPZ, Zn(DMP)2

Inputs

Flow	Cate...	Amount	Unit	Uncertainty	Provider
3-(N,N-dimethylamino)propyl magnesium chloride	SAL...	7.44140	g	none	3-(N,N-dimethylamino)propyl magnesium chloride
electricity, low voltage	351:...	7640.000...	J	none	market group for electricity, low voltage | electricity, low voltag
electricity, low voltage	351:...	0.18000	MJ	none	market group for electricity, low voltage | electricity, low voltag
electricity, low voltage	351:...	5721.633...	J	none	market group for electricity, low voltage | electricity, low voltag
electricity, low voltage	351:...	0.18000	MJ	none	market group for electricity, low voltage | electricity, low voltag
pentane	062:...	75.00000	g	none	market for pentane | pentane | Cutoff, S - GLO
tetrahydrofuran	201:...	44.40000	g	none	market for tetrahydrofuran | tetrahydrofuran | Cutoff, S - GLO
Zinc Chloride	SAL...	3.47000	g	none	Zinc Chloride

Outputs

Flow	Category	Amount	Unit	Costs/Rev...	Uncertainty	Avoided ...	Provider	Data quali...	Location	Description
BDMPZ, Zn(DMP)2...	**SALD/chemicals**	**3.80000**	**g**		**none**					

Figure S10: LCA detail: Synthesis of $Zn(DMP)_2$

Crystallographic study of AgNW/ZnO nanocomposites using SAED

By analogy to standard X-ray diffraction (XRD), where diffraction peaks can be identified at various 2θ values, corresponding to the angle between the incident ray and the corresponding diffracted ray, diffracted peaks are expected to appear along concentric diffraction rings in the case of selective area electron diffraction (SAED) patterns at specific scattering vectors Q, which are conventionally related to XRD peaks (using X-rays with a wavelength λ) as

Equation 6

$$Q = \frac{2\sin\theta}{\lambda}.$$

These rings can be traced out for the typically expected diffraction peaks of ZnO and metallic Ag as per the ICDD database sheets to give Figure S19 in the case of the 320 ALD cycle-coated AgNW sample. Sharp localized diffraction peaks were found at Q values corresponding to the cubic metallic Ag phase, indicating this phase was monocrystalline, while concentric rings were found for almost all Q values corresponding to ZnO. The presence of concentric rings in lieu of localized diffraction peaks reflects the large variety of crystal orientations present around the AgNW, and shows the coating was polycrystalline. The concentric ring associated to the 002 peak of ZnO was found to be quite weak, which may be attributed to the preferential a-axis growth of these coatings.

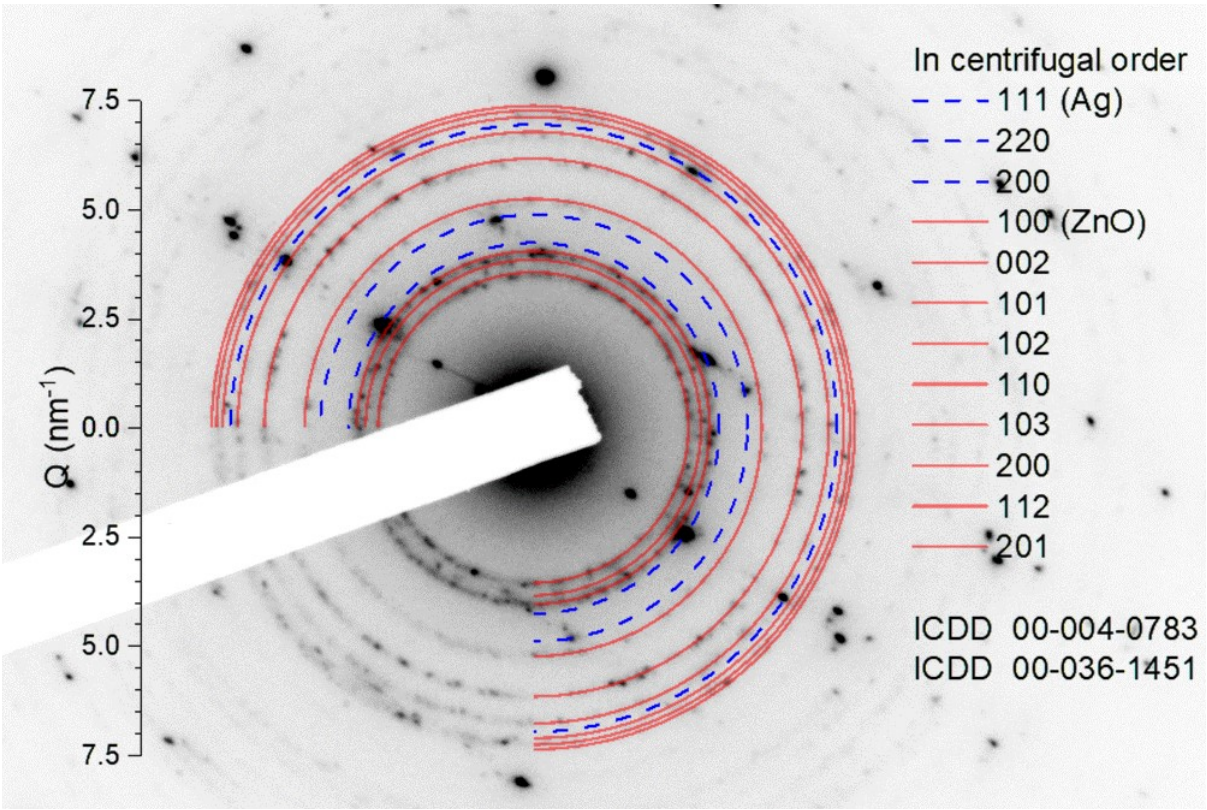

Figure S11: SAED of single AgNW coated with 320 cycles of $Zn(DMP)_2/H_2O$ SALD at 150 °C. Concentric circles have been traced out at all possible diffraction scattering vectors up to 7.5 nm^{-1} for ZnO and metallic Ag.

AgNW/ZnO nanocomposites characterization

A slight uptick in resistance was observed in the sample coated with 320 ALD cycles after an applied voltage of around 7 V, but is likely due to a local crack propagation phenomenon and not to a more global heat-induced spheroidization which did happen later at 10.3 V and rendered the network non-percolating at a value consistent with previous DEZ experiments.[8]

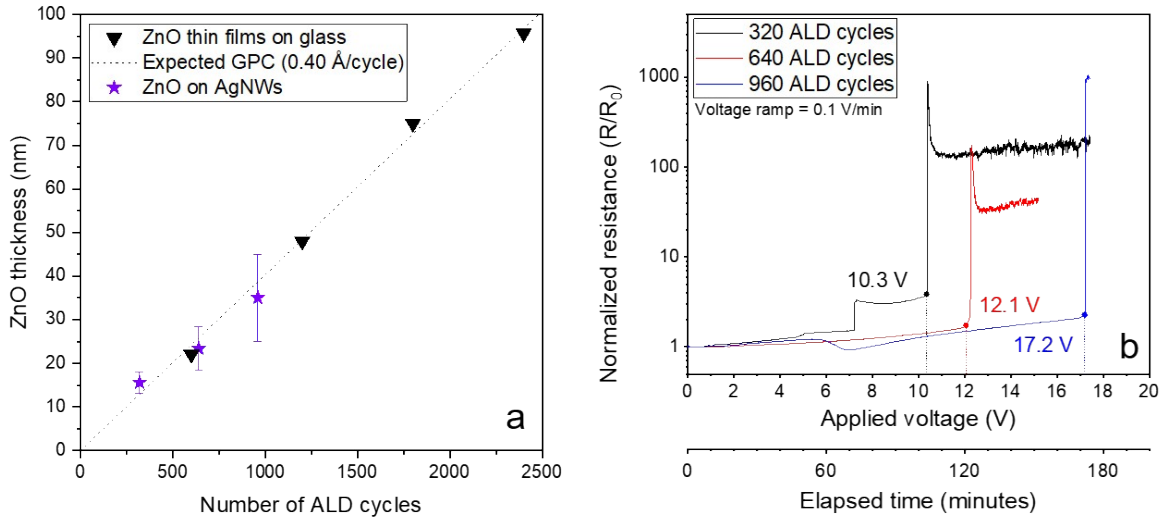

Figure S12: ZnO shell thickness estimated from BS SEM (see Figure 7-B1, B2, and B3) vs. number of ALD cycles, compared with growth of thin films on glass through the same approach (a). Evolution of normalized resistance vs. applied voltage and determination of AgNW network breakdown voltage vs. number of ALD cycles coated (b).

DEZ and $Zn(DMP)_2$ pyrophoricity test

Figure S13 reports images following the exposure of both DEZ and $Zn(DMP)_2$ to air. DEZ reacted instantaneously, whereas $Zn(DMP)_2$ reacted slowly and without producing a flame. $Zn(DMP)_2$ was submerged in water after 2 minutes of contact with air to accelerate the reaction, and still no flame was observed, though a momentarily audible hissing sound confirmed the reaction was still ongoing. This demonstrates $Zn(DMP)_2$ does not self-ignite upon exposure to air, even in high humidity environments and after extended periods of time, making $Zn(DMP)_2$ non-pyrophoric.

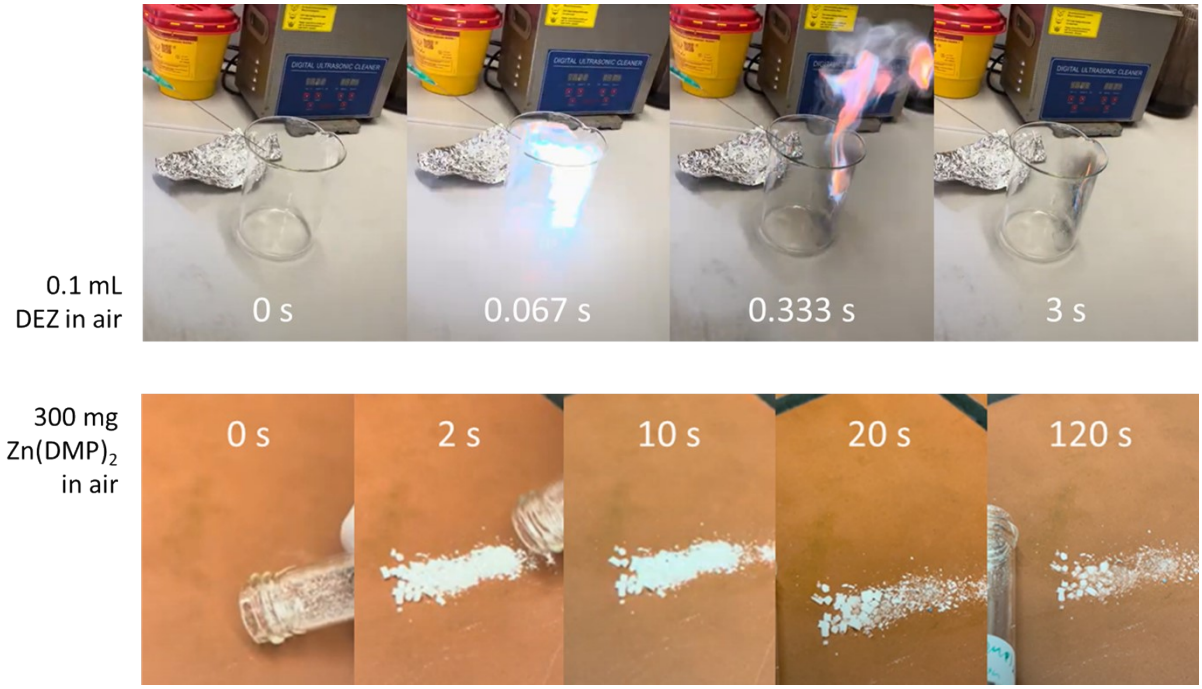

Figure S13: Exposure of DEZ (top) and $Zn(DMP)_2$ (bottom) to air. DEZ violently and instantaneously reacted forming a flame which was much larger than the DEZ volume before reaction (0.1 mL); $Zn(DMP)_2$ produced no flame upon reaction with air, even after 2 minutes.

References

1 P. Poodt, A. Mameli, J. Schulpen, W. M. M. (Erwin) Kessels and F. Roozeboom, *J Vac Sci Technol*, 2016, **35**, 021502.

2 U. Pietsch, V. Holý and T. Baumbach, in *High-Resolution X-Ray Scattering: From Thin Films to Lateral Nanostructures*, eds. U. Pietsch, V. Holý and T. Baumbach, Springer, New York, NY, 2004, pp. 143–178.

3 T. Muneshwar and K. Cadien, *J. Appl. Phys.*, 2018, **124**, 095302.

4 L. Mai, F. Mitschker, C. Bock, A. Niesen, E. Ciftyurek, D. Rogalla, J. Mickler, M. Erig, Z. Li, P. Awakowicz, K. Schierbaum and A. Devi, *Small*, 2020, **16**, 1907506.

5 M. A. Curran, *US EPA Life Cycle Assessment: Principles and Practice.*, 2006.

6 M. F. K. Niazi, D. Muñoz-Rojas, D. Evrard and M. Weber, *ACS Sustain. Chem. Eng.*, 2023, **11**, 15072–15082.

7 C. Bauer, J. Buchgeister, R. Hischier, W. R. Poganietz, L. Schebek and J. Warsen, *J Clean Prod*, 2008, **16**, 910–926.
8 A. Khan, V. H. Nguyen, D. Muñoz-Rojas, S. Aghazadehchors, C. Jiménez, N. D. Nguyen and D. Bellet, *ACS Appl. Mater. Interfaces*, 2018, **10**, 19208–19217.